



Oxidation state of Mo affects dissolution and visible-light photocatalytic activity of MoO₃ nanostructures



Janire Peña-Bahamonde^a, Chunzheng Wu^b, Sofia K. Fanourakis^c, Stacey M. Louie^a, Jiming Bao^b, Debora F. Rodrigues^{a,c,*}

^a Department of Civil and Environmental Engineering, University of Houston, Houston, TX 77204-4003, United States

^b Department of Electrical and Computer Engineering, University of Houston, Houston, TX 77204-4003, United States

^c Department of Materials Science and Engineering, University of Houston, Houston, TX 77204-4003, United States

ARTICLE INFO

Article history:

Received 14 August 2019

Revised 14 November 2019

Accepted 23 November 2019

Available online 14 December 2019

Keywords:

MoO₃

Nanorods

Nanoplates

Nanowires

pH dependency

Dissolution

Reactive oxygen species

ABSTRACT

The role of shape, dissolution, and chemical properties of MoO₃ nanomaterials with visible light photocatalytic activity are still largely unknown. In the present study, we investigate the photodegradative properties and role of dissolution products under different pH values of three MoO₃ nanomaterials with different shapes and chemical properties (nanorods, nanowires, and nanoplates). We show that different morphologies of MoO₃ present different solubility behaviors with increasing pH (with the highest solubility occurring at pH 10), and this dissolution depends on the oxidative state and nature of the Mo–O bonds, not just the size and morphology of the nanostructures. Nanoparticle dissolution seems to favorably affect the discoloration rate of methylene blue (MB) but not its photocatalytic degradation. It is important to differentiate MB discoloration as opposed to photocatalytic degradation since discoloration involves not only photocatalytic degradation but also adsorption and ion complexation processes. Our experiments for the removal of MB show that the nanorods present the best photocatalytic-based degradation activity, while the nanowires, which present the highest dissolution, decolorize MB the fastest. MoO₃ photocatalytic degradation mechanism was investigated via the quantification of nanoparticle-produced reactive oxygen species (ROS) and measurement of MB photocatalytic degradation inhibition due to the presence of ROS scavengers. According to the results, photogenerated holes in the nanomaterial govern the degradative process by allowing production of hydrogen peroxide. This study demonstrates that MoO₃ nanostructure chemical and physical properties, as well as nanostructure dissolution process, influence the photocatalytic properties of MoO₃ nanostructures.

© 2019 Elsevier Inc. All rights reserved.

1. Introduction

Recently, MoO₃ nanostructures have been described to present photocatalytic properties under visible light. Degradation of methylene blue [1,2] and orange II dye [3], methanol oxidation [4], epoxidation [5], gas sensing properties [6], supercapacitor [7], optical properties [8], and lithium storage capabilities [9] have been investigated with MoO₃ under visible light. The photocatalytic performance of MoO₃ has been associated to shape, size, and chemical properties. Different synthetic strategies have shown that MoO₃ exhibits *h*- and α - phases [10]. The *h*-phase corresponds to nanorods morphologies while the α - phase corresponds to nanoplates and nanowires [11–13]. Control of the morphology and

nanoparticle size can be achieved by varying different parameters, e.g. the concentration of reactants, time, temperature, pressure, and solvents. Despite the fact that visible light photocatalysis makes MoO₃ an attractive material for contaminant degradation, prior studies have demonstrated that dissolution of MoO₃ can occur in aqueous systems [14–16] diminishing its utility for water treatment and other applications. However, a thorough study of the dissolution and photocatalytic activity of the various phases and morphologies of MoO₃ nanostructure has not yet been conducted, to our knowledge.

Many studies have shown that other types of nanoparticles, including silver [17,18], silica [19], ZnO [20,21], and CeO₂ [21] nanoparticles (NPs) can dissolve. The stability of the nanoparticles in terms of dissolution will depend on several factors such as presence of natural organic matter, ionic strength, and type of electrolyte, aggregation state, pH, and size [22]. In the case of organic matter, the dissolution can be increased or decreased by steric

* Corresponding author at: Department of Civil and Environmental Engineering, University of Houston, Houston, TX 77204-4003, United States.

E-mail address: dfrirodrigues@uh.edu (D.F. Rodrigues).

shielding or ligand-promoted processes, respectively. When ionic strength, type of electrolyte, or pH are altered, the behavior of the particles can also change and lead to increased nanoparticle aggregation, influencing the exposed surface area to the media and dissolution. Size can also play a role, whereby smaller particles are more prone to dissolving than larger particles, as described by the well-known Ostwald-Freundlich equation. In the case of MoO_3 , it has been shown, that pH changes can play an important role in the dissolution of this nanoparticle [14]. Dissolution of the NPs can be expected to change the heterogeneous catalytic reactions that occur at the NP surface and perhaps even affect the production of reactive oxygen species (ROS). The dissolution behavior of the nanoparticles is critical in determining both the toxicity and reactivity of the nanoparticles. This phenomenon will also be harmful in water treatment not only due to the toxicity effect of the dissolved ions but also because the catalytic process that consumes the catalyst are typically cost-prohibitive.

Previous investigations have shown that the production of reactive oxygen species (ROS) play an important role in photocatalytic reactions. The quantification of individual ROS is a prerequisite to elucidate actual ROS functions in photocatalysis. The production of different ROS by TiO_2 [23–26], graphene oxide [27], silver [28], ZnO [26,29], and iron oxide [30] is well studied. However, the production of ROS by photocatalysts induced by visible light, specifically MoO_3 , have not been reported thus far. In the present study, we take into consideration the role of pH in the dissolution of MoO_3 nanostructures as well as the effects of dissolution in ROS production and degradation of methylene blue (MB), as an example of a water contaminant, to understand the mechanisms of the photocatalytic degradation of MoO_3 nanostructures. We hypothesize that MoO_3 nanostructures with different material properties will show different propensities to dissolve, and that the dissolution behavior will then change the photocatalytic ability of the NPs.

2. Materials and methods

2.1. Materials

Ammonium molybdate tetrahydrate ($(\text{NH}_4)_6\text{Mo}_7\text{O}_{24}\cdot 4\text{H}_2\text{O}$), nitric acid (HNO_3), molybdenum powder (1–5 μm , $\geq 99.9\%$), hydrogen peroxide (H_2O_2), ethanol (EtOH), methanol (MeOH) HPLC grade, furfuryl alcohol, terephthalic acid, isopropanol ($>99.7\%$), benzoquinone (AR grade), triethanolamine ($>99.0\%$) and methylene blue were purchased from Sigma-Aldrich and were used as received. Glutathione and 5,5'-Dithiobis (2-nitrobenzoic acid) (Ellman's reagent) were supplied by Fisher Scientific.

2.2. Synthesis

The MoO_3 nanomaterials were synthesized by the hydrothermal route using modified published procedures [3,31,32]. Briefly, the modifications were: the nanorod MoO_3 nanostructure were prepared by dissolving 2.46 g of $(\text{NH}_4)_6\text{Mo}_7\text{O}_{24}\cdot 4\text{H}_2\text{O}$ in 20 mL of distilled water (DIW). To this solution, 5 mL of HNO_3 was added drop by drop. The solution was transferred to an 80 mL Teflon-lined stainless-steel autoclave and heated at 90 °C. After 3 h of reaction a white precipitate was collected and washed several times with EtOH (70%) and then dried at room temperature.

Black MoO_{3-x} nanoplates and nanowires were prepared according to the procedures reported by Yin et al. [32] with some modifications. For the nanoplates, 192 mg of molybdenum powder was added to a Teflon vessel (45 mL) containing 24 mL of ethanol under magnetic stirring. Then, 3 mL of H_2O_2 (30%, from Macron Fine Chemicals) was injected, and the mixture was stirred for 0.5 h to obtain a yellow solution. The Teflon vessel was then sealed in a

stainless-steel autoclave, heated, and maintained at 160 °C for 14 h. The product was collected by centrifugation, washed with ethanol several times, and finally dried under vacuum. The nanowires were prepared using the same procedure as the black nanoplates except using 384 mg of molybdenum powder, 30 mL of isopropanol, and 5 mL of H_2O_2 (30%, from Macron Fine Chemicals).

2.3. Nanomaterial characterization

Crystallographic information of samples was determined by X-ray diffraction (XRD) (Philips X'pert Pro X-ray diffractometer). The Cu K α radiation was used ($\lambda = 1.54 \text{ \AA}$) at a scanning rate of 0.020° per second from 5° to 80° in 2 θ . The voltage was set to 40 kV, and the current to 40 mA. Crystal sizes of the samples were estimated from the full-width at half-maxima (FWHM's) of some intense XRD diffraction peaks using Scherrer's method.

Fourier-transform infrared spectroscopy (FTIR) was performed in a Thermo Scientific Nicolet IS50 FTIR Spectrometer in the wavenumber range from 4000 to 500 cm^{-1} . The ATR-FTIR was employed to evaluate the interaction between MB- MoO_3 and MB-ion. After each reaction, samples were centrifuged for collection of the pellet, which were subsequently freeze-dried. The spectra were obtained on a Digilab FTS 7000 equipped with a HgCdTe detector from 4000 to 600 cm^{-1} wavenumbers.

The morphology of crystal samples was examined by scanning electron microscopy (SEM). Samples were coated with gold for 30 s (Denton Desk V) and then, observed by SEM (Nova NanoSEM 230) at accelerating voltage equal to 5 kV at different magnifications. The size of the nanomaterials was estimated using ImageJ. MATLAB 2018a was used to generate histograms and determine the average particle sizes.

The Brunauer–Emmett–Teller (BET) surface area for all nanomaterials were measured by N_2 physisorption using a Micromeritics-3FLEX and standard multipoint BET analysis methods. Prior to analysis, 0.2 g of powder were degassed on Micromeritics-Smart VacPrep at a 120 °C for 24 h.

X-ray photoelectron spectroscopy (XPS) was performed in a PHI Quantera SXM Scanning X-ray Microprobe with Al K α (1486.6 eV) as the excitation source. The binding energy was calibrated by setting the adventitious carbon (corresponding to C-C bonds) to 284.8 eV. High-resolution spectra were acquired with a pass energy of 23.5 eV, an energy step size of 0.2 eV, and a time step of 50 ms.

Energy band gap measurements were performed by UV–vis Diffuse Reflectance Spectroscopy (UV–vis DRS) and were recorded in a Hitachi UV–vis Spectrophotometer U-2001 using BaSO_4 as the reference. The bandgaps were determined based on the Kubelka-Munk function: $F(R) = (1 - R)^2/2R$.

Zeta-potential measurements were performed in a Zetasizer Nano (Malvern) using the zeta potential transfer standard DTS 1235. The samples were measured with 100 mg/L of each nanomaterial at pH values varying from 2 to 10, adjusted with either HCl or NaOH.

2.4. Dissolution measurements of MoO_3 nanostructures at different pH values

Dissolution experiments were conducted at different pH values (2, 5, 7 and 10) and at room temperature ($\approx 25 \text{ }^\circ\text{C}$). A mass of 10 mg of MoO_3 nanostructure was dispersed in 30 mL of deionized water with adjusted pH using either HCl or NaOH prior to the addition of the nanostructures' dissolution was evaluated for up to seven days (after 30 min, 1 h, 4 h, 6 h, 24 h, 48 h, 96 h, and 168 h in solution). For each time point, a 5 mL sample was taken and filtered with 0.2 μm Nylon filters, and then centrifuged using Amicon ultrafiltration devices (30,000 NMWL) to ensure that all

solid particles were removed from the solution. After the filtration, the solutions were measured by flame atomic adsorption spectrometry (AAS) (AAAnalyst 200, Perkin Elmer) using a Molybdenum lamp from Perkin Elmer. Five standard solutions with known Mo concentrations were prepared as calibration standards. Exact concentrations of Mo in the sample solutions were obtained using the working calibration curve generated from the standard solution data. The averages and standard deviations of triplicate measurements were reported for all dissolution measurements. The supernatant of each experiment was collected and characterized by XPS and UV–vis, to determine the nature of the ion.

The isolated ions from the nanorods were also employed at a concentration of 500 mg/L for the evaluation of their interaction with MB using UV–Vis spectroscopy. The degradation of MB by the ions was investigated via HPLC. The ROS production by the ions followed the same procedures as the ROS production by the nanostructures as described below. The conditions and instrument settings used for the HPLC, ROS and UV–Vis were the same as described below for the nanostructures.

2.5. Photocatalytic activity experiments

Photocatalytic experiments were carried out at different pH values, varying from 2 to 10 to measure the amount of discoloration of methylene blue (MB) in aqueous suspensions of MoO₃, which were exposed to visible light (Nexlux LED light, which utilizes the 5050 RGB LED package with a wavelength range of 400–700 nm and maximum luminous intensities of 100, 400, and 100 mcd for the red, green, and blue regions, respectively). The initial concentration of MB was fixed at 50 mg/L with a catalyst loading of 500 mg/L and a final volume of 20 mL. Prior to photooxidation, the solution was stirred in the dark for 30 min to establish an adsorption–desorption equilibrium [2,33]. During irradiation, 1 mL of the mixture solution was withdrawn every 30 min, and then centrifuged (Thermo Scientific Sorvall Legend XTR Centrifuge) at 10,000 rpm for 10 min to separate photocatalysts from the mixture. The extent of MB removal was determined by measuring the absorbance values on a UV–Vis spectrometer using a SynergyMX Microtiter plate reader (Biotek) at $\lambda = 664$ nm. The experiments were performed in triplicate. The results were analyzed and reported as discoloration of MB or MB photocatalytic degradation. The data for the MB discoloration in the light included both adsorption of MB to the nanoparticle, complexation of MB with the dissolved MoO₃ ion, and photocatalytic degradation. For the discoloration in the dark, any MB discoloration reported corresponded to adsorption of MB to the nanoparticle and complexation with the ion. In both conditions, dark and light, we needed to consider the complexation process between the dissolved MoO₃ ions and MB. In the case of photocatalytic degradation, the data corresponded to the true photocatalytic activity of the nanostructure. To obtain the true photocatalytic degradation, the discoloration of MB at the end of the light reaction (which included adsorption, complexation, and degradation) was subtracted from the MB discoloration at the end of the dark reaction (which included adsorption and complexation).

2.6. Reactive oxygen species detection

Reactive oxygen species (ROS) detection was evaluated from pH 2 to 10 by quantifying the production of different species. The concentration of singlet oxygen (¹O₂) was determined by monitoring the concentration of furfuryl alcohol (FFA), as previously described [27]. Hydroxyl radical (*OH) was evaluated by the analysis of the degradation of terephthalic acid [27]. The loss of thiol in glutathione (GSH) was used as an indirect method to measure hydrogen peroxide (H₂O₂) production by nanomaterials [34,35].

2.6.1. Loss of glutathione

MoO₃ nanostructures and ions, were investigated for hydrogen peroxide production in triplicate by measuring the loss of thiol in GSH. Briefly, 0.4 mM GSH was allowed to react for 2 h at room temperature with samples containing 500 mg/L of MoO₃ or [MoO₄]²⁻. Negative controls with non-oxidative agent (H₂O₂), and positive controls containing hydrogen peroxide (30%) were also measured. All the samples where tested in dark and light conditions, after which 100 mM of Ellman's reagent in Tris-HCl 100 mM was introduced into each tube and allowed to react for 10 min. Then, the nanostructures were removed by filtration using a 0.2 μ m syringe filter (Corning, U.S.A.). The absorbance of the filtrate was read at 412 nm using a Synergy MX Microtiter plate reader to measure the loss of thiols. The results were expressed as the loss of GSH and represented by Eq. (1) [34].

$$\text{ROS production (\%)} = \frac{\text{Negative control absorbance} - \text{Sample absorbance}}{\text{Negative control absorbance}} \times 100 \quad (1)$$

2.6.2. Hydroxyl radical

The production of hydroxyl radical was evaluated via the analysis of the hydroxylation of terephthalic acid (TA) to form fluorescent species. The fluorescent species of 2-hydroxyterephthalic acid was measured at 425 nm in the Synergy MX Microtiter plate reader. Negative controls (without MoO₃) and positive controls (TA) were also analyzed. A concentration of 500 mg/L of the nanostructures or [MoO₄]²⁻ were allowed to react with 2 mM of TA. After 2 h, the nanostructures were removed by filtration with 0.2 μ m nylon filters, and the 2-hydroxyterephthalic acid generated in the samples were quantified by fluorescence using a Synergy MX Microtiter plate reader. The fluorescence intensity was read at an emission wavelength of 425 nm in the fluorescence spectra for 312 nm excitation wavelength [27,36,37]. The results were expressed using Eq. (1).

2.6.3. Singlet oxygen

Singlet oxygen species were evaluated from previously reported methods [38,39]. Briefly, 500 mg/L of each nanoparticle or the isolated ion were mixed with 0.5 mL of furfuryl alcohol (10 μ M). Positive and negative controls without nanostructures were analyzed. When the reaction was completed, after 2 h, the nanostructures were removed by filtration using 0.2 μ m nylon filters and analyzed by high performance liquid chromatography (HPLC). The chromatographic measurements were carried out on a HPLC Agilent Technologies 1290 Infinity with a Zorbax Eclipse Plus C18 4.6 \times 150 mm, 5 μ m column. The mobile phase was H₂O:MeOH (80:20)%. The flow rate was 1 mL/min, and the injection volume was 20 μ L. The concentration of ¹O₂ was calculated by the integration of the peak area for $\lambda = 219$ nm observed at a retention time of 2.6 min in the chromatographs and expressed by Eq. (1).

2.7. Product analysis and identification

The MB and its degraded products were separated and identified based on the literature [40]. The MB degradation products were analyzed and separated on the HPLC system described above, with the UV–vis diode array detector set to record the absorbance at 600 nm. The mobile phase was made from acetonitrile (solution A) and buffer solution (solution B). The buffer solution was 0.1 M ammonium acetate and acetic acid (pH 5.3). The gradient elution was a linear gradient from 5% A to 95% A in 30 min, at a total flow rate of 0.8 mL/min, and the injection volume was 100 μ L.

2.8. Scavenger experiments

Isopropyl alcohol (IPA), triethanolamine (TEOA) and p-benzoquinone (p-BQ), were added to the reaction in order to evaluate the degradation mechanisms. The experiments were performed for the nanorods at pH 5.4 employing the same procedure as the one described in the photocatalytic activity experiments. Briefly, 50 mg/mL of MB with 500 mg/L of the nano-material in a final volume of 20 mL was prepared. To each reaction, 10 mM of TEOA, 75 mM of IPA and 1 mM of p-BQ were employed. After 30 min stirring in the dark to establish an adsorption-desorption equilibrium, the samples were irradiated. An aliquot of 1 mL of sample was collected every 30 min and then centrifuged. The absorbance at $\lambda = 664$ nm was measured to analyze the discoloration of MB.

3. Results and discussion

3.1. Synthesis and characterization of the nanostructures

Three MoO₃ nanostructures with different morphologies were successfully synthesized, as shown in Fig. 1. All the nanostructures showed smooth surfaces, as well as regular and monodisperse shapes and structures. The nanowires and nanorods presented diameters in the range of 59 nm and 180 nm, respectively. The nanoplates had a thickness around 74 nm and a width of approximately 180 nm. Both the nanorods and nanowires presented lengths greater than 5 μ m.

The chemical and crystalline structures of the nanostructures were determined by XRD, FT-IR spectroscopy, and XPS. XRD

patterns for the MoO₃ nanostructures are shown in Fig. 2. The strong diffraction peaks demonstrate that the samples are highly crystalline. For the nanoplates and nanowires most of the peaks were indexed as orthorhombic MoO₃ (JCPDS – 35–0569) and for the nanorods as hexagonal (JCPDS – 21–0569). Using the Scherrer equation [41,42] and the FWHMs, the crystal sizes of the nanowires, nanoplates, and nanorods were calculated to be 32 nm, 29 nm, and 33 nm, respectively. The difference in sizes with those of the extrapolated sizes from the SEM images could be due to peak broadening caused by crystal lattice strain or lattice defects [43–45].

The specific surface areas of the prepared MoO₃ nanostructures are presented in Table 1. The surface areas obtained were 28.5 m²/g, 26.1 m²/g, and 1.1 m²/g for the nanoplates, nanowires, and nanorods, respectively. Comparatively, the different MoO₃ nanostructures obtained showed different surface areas, which was inversely proportional to the nanostructure sizes.

The normalized FT-IR spectra of the MoO₃ nanostructures were done at wavenumbers 520, 537, and 564 cm⁻¹ for the nanorod, nanowire, and nanoplate spectra, respectively, and are shown in Fig. 3. The peaks around 972, 969, and 984 cm⁻¹ were associated with the Mo=O stretching vibration. The peaks around 896, 708, and 840 cm⁻¹ were associated with the Mo–O–Mo stretching, and the peaks at 517, 555 and 538 cm⁻¹ were the result of the O–Mo₃ single bonds [46–48]. The weak peaks located around 1400 and 1600 cm⁻¹ were related to the presence of the crystallization of water in the crystals of the MoO₃ nanostructures. The nanorods showed peaks in the 800–1000 cm⁻¹ and 500–600 cm⁻¹ ranges indicating presence of the Mo=O bond and Mo–O bonds, respectively. Similarly, the nanoplates presented both bond types as the nanorods. However, the nanowires seemed to have an

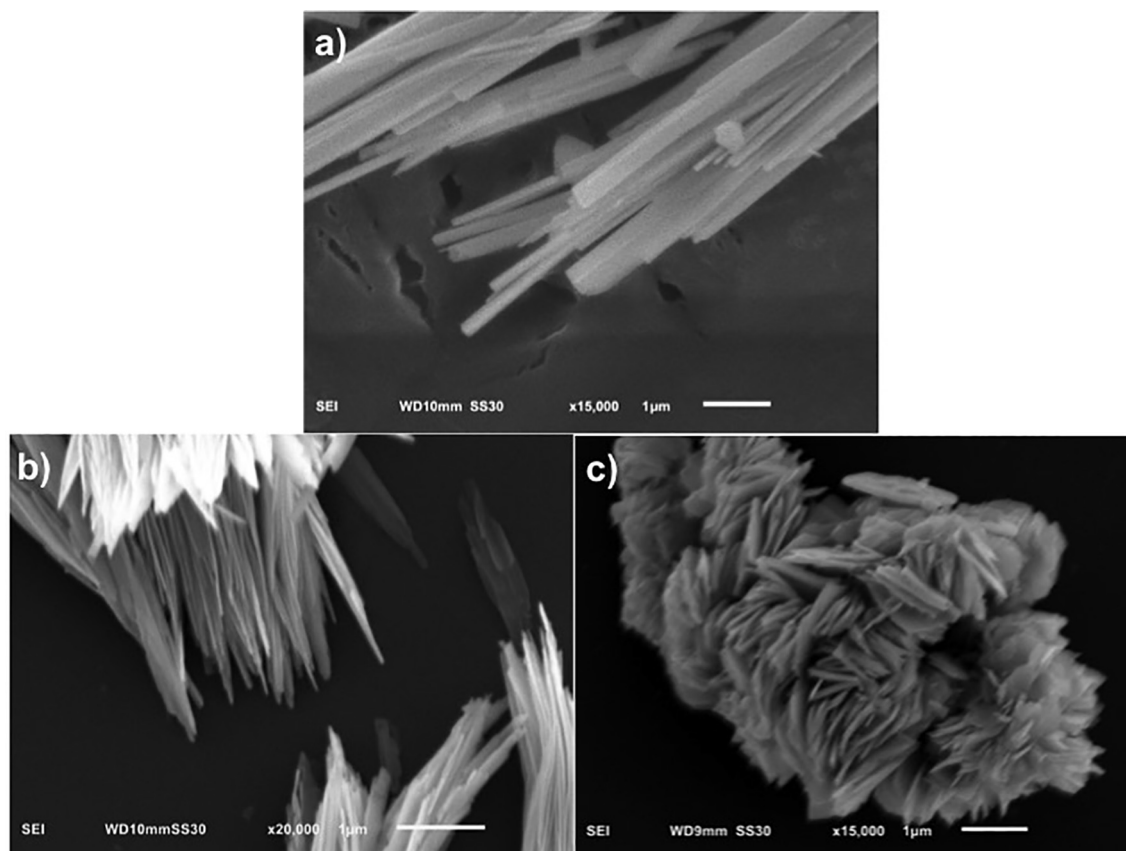


Fig. 1. SEM images of (a) nanorods (b) nanowires and (c) nanoplates. The scale bars correspond to 1 μ m size.

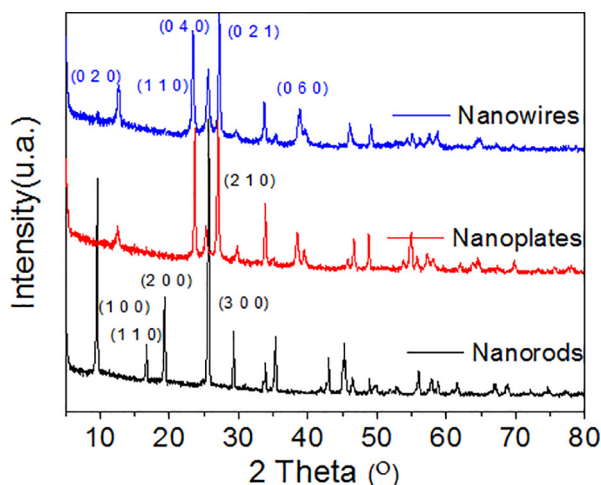


Fig. 2. XRD of the MoO₃ nanostructure.

increased presence of single bonds as observed with the 538 nm peak. The nanoplates did not have such a strong presence of the Mo—O single bonds. The Mo=O to Mo—O ratios shown in Table 1 confirmed this analysis since the nanowires double bond to single bond ratio was nearly half of that of the nanorods and nanoplates. Furthermore, the Mo—O—Mo peak in the nanoplates was shifted compared to the nanowires and nanorods, which was potentially caused by lattice distortion since the nanoplates have a significantly higher concentration of oxygen vacancies [49] than the other two nanomaterials, as shown in Fig. 4.

The surface chemistry of the nanostructures as well as the chemical states of the MoO₃ nanostructures were analyzed by XPS, as shown in Fig. 4. The Mo 3d spectra for all the nanostructures present different oxidative states. The spectrum for the nanorods showed presence of the binding energy (E_B) (Mo ³d_{5/2}) = 233.15 eV and E_B (Mo ³d_{3/2}) = 236.3 eV corresponding to Mo⁶⁺; however, the spectra of nanowires and nanoplates exhibited the presence of the peaks (Mo ³d_{5/2}) = 231.78 eV and E_B (Mo ³d_{3/2}) = 234.92 eV, which indicated the existence of Mo⁵⁺. Table S1 shows all the fitting parameters of the XPS spectra for all the nanomaterials. In Table 1, the calculation of the ratio of peak/area is shown. As we can see, the different morphologies showed different fractional amounts of Mo⁶⁺ and Mo⁵⁺, indicating that the nanostructure with a higher amount of Mo⁵⁺ contained large quantities of oxygen (O) vacancies, which have been introduced during the synthesis of the nanomaterial. Typically, the presence of these vacancies causes a deficiency of O in the crystal structure, which causes a decrease in the energy band gap [50] as evident in Table 1. This decrease in the energy band gap is desirable as previous studies have shown that it can increase the photocatalytic properties of the material by allowing greater absorption of light [51]. The bandgaps of all three material were less than 3 eV (Fig. S1) making the material capable of generating photoexcited electrons via the absorption of visible or UV light, especially considering that the nanowires and nanoplates were able to absorb light due to their localized surface plasmon resonance. The heavily

doped nonstoichiometric molybdenum oxide (MoO₃) is a typical and primary member of plasmonic semiconductors. It shows intense and tunable plasmonic resonance across the visible and NIR regions [52–54]. Due to the presence of oxygen vacancies (highly self-doped) and the free electrons, the dark MoO_{3-x} samples always show a plasmonic absorption in the vis-NIR region. This kind of absorption peak has been observed in our nanowire samples (Fig. S1b, peak at above 800 nm). However, due to the limited sensitivity of our device, it is not possible to identify the plasmonic absorption of the nanoplates sample, which is the darkest one and it absorbs almost all the visible light. While from the XRD patterns the nanowires and nanoplates appeared to have similar crystal structures, in the XPS the nanowires and nanorods appeared chemically more similar. This could be a result of the growth mechanism during synthesis resulting in different O vacancies in each nanostructure. Based on these results, the composition of the nanorods and nanowires nanostructures was similar regarding the oxidation states, however their structure was different due to the different growth mechanisms during synthesis. The differences in the chemical and physical structure of these nanomaterials could affect their stability, which is discussed later based on the dissolution stability of the different MoO₃ nanostructures. Furthermore, the differences in the morphology, surface area, and oxidative state, enhance the probability of the electron transition from Mo⁵⁺ valence band to Mo⁶⁺ conduction band.

3.2. Stability of MoO₃ nanostructures in aqueous solutions

Previous studies have described that the dissolution rate of nanoparticles can be affected by the size, crystallinity, shape, surface area, and exposed plane, among other factors [22]. The dissolution of the MoO₃ nanostructures was analyzed from pH 2–10 for a period of 1 week, as shown in Fig. 5. Interestingly, for all the nanostructures, the dissolution was only partial, *i.e.*, the nanostructures did not dissolve completely (*i.e.*, up to 100 mg/L of MoO₃ was dissolved) and eventually reached a plateau. The nanowires dissolved the most (*e.g.*, around 80% (260 mg/L of MoO₃) after 1 week at pH 10), compared to the nanoplates, which presented the lowest dissolution (<20% at all pH conditions). These results seem to be directly correlated to the presence of the Mo—O single bonds and double bonds, as well as the different oxidative states. For instance, the nanowires presented the highest dissolution as well as the strongest presence of Mo—O single bonds as seen in the FTIR results compared to the nanoplates (Fig. 3). In the case of the oxidative state, the nanoplates presented Mo⁵⁺ state as opposed to the nanowires and nanorods that had Mo⁶⁺ oxidative states and also higher dissolutions (Table 1).

Further analysis of the Mo ionic species dissolved through XPS and UV–vis spectroscopy (Fig. S2) showed that for all the nanostructures, the primarily dissolved ion was Mo⁶⁺. These results are in accordance with the literature that the majority of the dissolution of the nanostructures are with Mo⁶⁺ oxidative state (*e.g.* nanowires and nanorods) [55–58]. Aqueous solutions of Mo⁶⁺ ions have been studied in detail showing a dependency on the ion concentration and pH. The Pourbaix diagram of the Mo-system has been extensively studied and is used to study the stability of compounds

Table 1
Chemical properties of the three different MoO₃ nanostructures synthesized.

Nanostructure	Mean Size (nm)		$I_{\text{Mo-O}}/I_{\text{Mo=O}}$	Mo ⁶⁺	Mo ⁵⁺	Mo ⁶⁺ : Mo ⁵⁺ ratio	Surface area (m ² /g)	Energy bandgap (eV)
	From SEM	From XRD						
Nanorods	180	32	0.77	95.3	4.7	20.3	1.1	2.84
Nanowires	59	29	0.48	86.5	13.5	6.4	26.1	2.95
Nanoplates	74	33	0.99	34.7	65.3	0.5	28.5	2.64

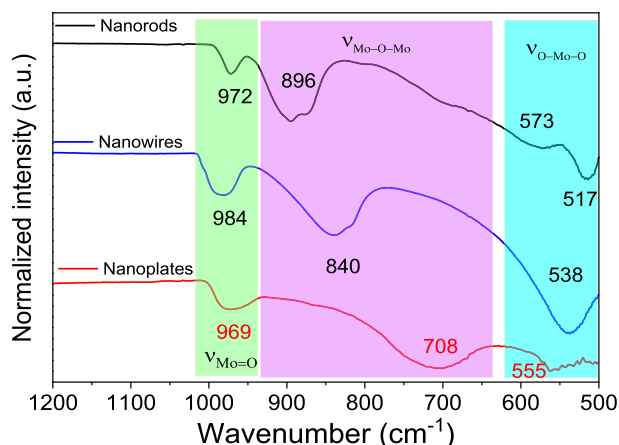


Fig. 3. FTIR spectra of the prepared nanostructures.

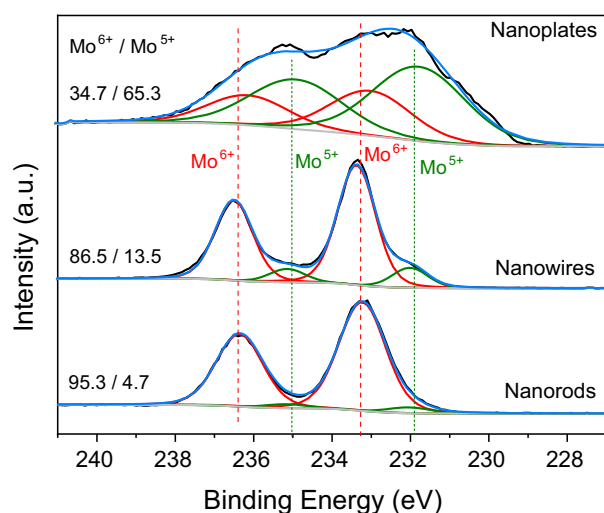
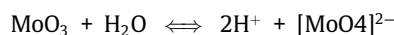


Fig. 4. XPS of all MoO₃ nanostructures.

in aqueous solutions. Generally, it is used to simplify complex reactions. Based on the Pourbaix diagram of Mo [59,60], at 25 °C, molybdate anion [MoO₄]²⁻ is formed when pH is higher than 4.2 and at -0.9 V. However, at acidic pH values, MoO₃ can be formed at -0.35 V. Different studies [14,60–63] about dissolution of MoO₃ coincide that the overall reaction is of the MoO₃ in aqueous solutions is



It is noteworthy to mention that MoO₃ dissolution is pH and temperature dependent and these structures are more stable at acidic pH rather than neutral and basic.

In our study, dissolution increased when the pH increased for all the nanoparticles. Furthermore, material dissolution was higher coincidentally with the increasing presence of Mo–O single bonds (*i.e.* nanowires > nanorods > nanoplates). These results suggest that the dissolution mechanisms can happen due to Mo–O single bonds since single bonds are more labile than double bonds.

In summary, the dissolution of the MoO₃ nanostructures depends on the pH of the media. The higher the pH is, the greater the dissolution. While it has been shown that nanoparticle dissolution is highly dependent on different factors, such as the crystal size and morphology, the extent by which the particles dissolve in solution, however, seems to be also dependent on the oxidation state and type of oxygen bonds found in the nanostructure [17].

3.3. MB Interactions with MoO₃ nanostructures

Initial investigation of the interaction of MB with the nanostructures was determined via ATR-FTIR (Fig. S3). The results showed that the nanostructure surface adsorbs MB. The differences between the ATR-FTIR spectra of the MoO₃ with MB in the dark and light showed the combination of bands of MoO₃ and MB and also a small shift to higher cm⁻¹ for some of the bands. For instance, the MB band at 880 shifted to 897 in the dark and to 884 in the light, and the MB band at 1596 cm⁻¹ shifted slightly to 1601 cm⁻¹ and 1602 cm⁻¹ for MB adsorbed to the nanostructure in the light and dark, respectively. To estimate the electric charge on the nanostructure surface and elucidate the ability of MB to adsorb onto the nanostructures, zeta potential measurements were performed. The magnitude of the zeta potential provides information about particle stability. Fig. S4 represents the zeta potential for all the nanostructure vs. pH. When the pH of the media increased, the zeta potential values for the nanorods and nanoplates decreased, while the zeta potential for the nanoplates increased slightly before decreasing slightly again. These patterns follow the degradation pattern due to light, as illustrated in Fig. S5, indicating that, due to the increasingly negative surface charge at higher pH values, the degradation decreases. This could be caused by the increased adsorbance of the MB (a positively charged molecule) to the nanostructure at higher pH values, which would decrease the ability of the nanostructure to absorb light. It could also be caused by the facilitated conversion of holes to hydroxyl radicals at high pH values [64]. Since the holes are more active

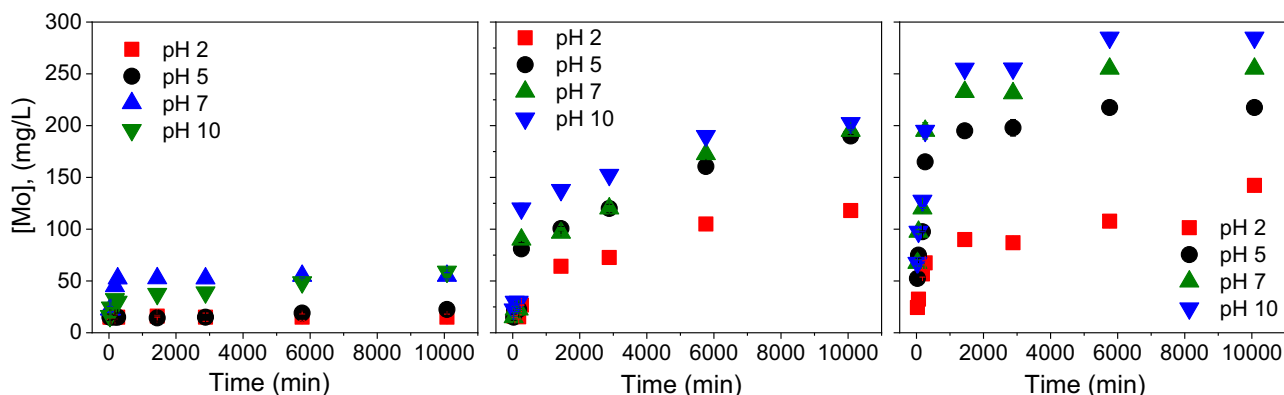


Fig. 5. Representation of Mo (mg/L) dissolved vs. time at different pH values. From left to right, in order of increasing dissolution, nanoplates, nanorods, and nanowires.

than hydroxyl radicals in this reaction, the conversion would result in a decline of the activity.

To verify whether degradation of MB or mere adsorption or complexation was taking place, XPS was utilized. The XPS results on the surface of the nanostructure (Fig. S6) showed a decrease in the pyridinic acid band when compared to the MB alone, indicating that photocatalytic degradation of MB is taking place. Furthermore, the decrease in the N quaternary was greater for the samples that were irradiated than for those kept in the dark.

The fact that all the nanostructures exhibit similar behavior with regards to their ability to decolorize MB; however, the evaluation of the degradation byproducts of MB was performed only for the nanorod MoO_3 . Fig. S5 shows the chromatographic separation of the methylene blue in dark and light conditions after 2 h of reaction at pH 5.4. The data showed that MB was significantly degraded under light irradiation, while some adsorption was observed when the reaction was placed in the dark. The decrease in the methylene blue peak intensity and the appearance of new peaks at lower retention times have been reported previously [64]. Consequently, photocatalysis of dye solutions not only caused its discoloration, but also an appreciable degree of transformation of the dye molecule.

In the case of the ions, the HPLC results of the reaction between the ions and methylene blue also showed some degradation byproducts. From the results, when the reaction was performed in the dark (Fig. S5 blue curve), the chromatograms did not show any peaks at lower retention times as opposed to light. The strong interaction between methylene blue and the isolated ions was confirmed with the ATR-FTIR spectra. In the spectra, it was possible to observe a decrease in the OH band for the ion-MB spectra, and the appearance of the MoO_3 band at 550 cm^{-1} (Fig. S7). This result showed that a MB-Mo ion complexation was happening during the reaction. Fig. S8 showed a blue precipitate when the ion was in contact with MB. The small contribution of the ions in the degradation process and the complexation observed by ATR-FTIR showed that both processes were happening simultaneously. That means that the peaks observed in the chromatogram are degradation byproducts and not complexes. These results confirm that the ions were also participating in the degradation process.

3.4. Photocatalytic activity of the nanostructures and ions with MB

In this investigation, we tried to understand the role of the nanostructures' characteristics in relation to their ability to decolorize MB, *i.e.* simultaneous adsorption, ion-MB complexation, and photocatalytic activity, and true photocatalytic activity (Fig. 6). In the discoloration assay (Fig. 6), adsorption, complexation with the ion, and photocatalytic phenomena were reported for the light exposure, while in the dark only adsorption and ion complexation were observed. Fig. S9 shows the relative emission intensity of the lamp and the MB absorbance spectra. There is a small overlap in the emission wavelengths of the LED light and the absorbance of MB. While MB is capable of absorbing some of the light emitted by the LED light, it does not influence the absorption of the nanostructure, as the majority of the light emitted by the lights falls outside the region of light absorbance by MB (Fig. S9). In the case of the photocatalytic percentage discoloration (Fig. 6), the photocatalytic activity, after subtraction of the discoloration reaction of MB in the dark and light conditions, was reported to show the amount each material was able to decolorize solely due to the influence of the light exposure, *i.e.* photocatalysis (Fig. 6). All three materials were able to decolorize MB as shown in Fig. 6, however, the nanorods displayed greater photocatalytic percentage discoloration, therefore was considered to have the best photocatalytic activity. While the nanowires displayed the fastest discoloration

activity due to the influence of their increased dissolution, they displayed the least photocatalytic activity.

In the case of the rate of discoloration of MB, herein defined as the time it took for each nanomaterial to decolorize MB, shown in Fig. 6 as the final timepoint of each discoloration experiment. The results show that the nanowires had the fastest reaction rate, which was capable of decolorizing MB after 90 min. The nanorods, on the other hand, decolorized MB after 210 min, and the nanoplates after 300 min. The rate at which each nanostructure decolorized MB could be explained in terms of the stability of the nanostructure. The nanowires, which were the particles that showed the highest dissolution, were the ones showing the highest reaction rate.

These results indicated that the photocatalytic activity of the material was not directly or completely related to the band gap energy of the material or the relative percentages of the different oxidation states of the Mo (Table 1). The nanorods presented the highest photocatalytic activity, while they had the second largest band gap and the largest ratio of Mo^{+6} to Mo^{+5} ions. The nanoplates presented the lowest photocatalytic activity, even though they had the smallest bandgap and smallest ratio of Mo^{+6} to Mo^{+5} ions. This indicates that while a smaller band gap can be beneficial in allowing greater absorption of light, the more defects and absorption of visible light by mid-gap states may not be efficient for exciton generation. Hence, based on these results, the oxidation state seems to be also playing a significant role in the material's photocatalytic properties.

In order to confirm the role of dissolution on the photocatalytic activity, the photocatalytic degradation results of MB by the nanostructures were compared against the nanostructure dissolution at the end of each reaction at different pH values as shown in Fig. 7 to understand the role of dissolution on degradation of MB. Increasing the pH from 2 to 10 resulted in enhanced dissolution of the nanorods and nanowires by 40% and 60%, respectively, which was accompanied by an increased decolorization of MB. However, the difference in dissolution of the nanoplates did not show a detrimental impact on the degradation of MB, likely because of the lower extent of dissolution of the nanoplates (<20% at all pH values over the experimental period). These results showed that the more dissolution exhibited by the nanostructure, the less degradation of MB was observed. This can be due to a competition mechanism between the ion and the nanomaterial. While the nanostructure is dissolving, a competition between ion-MB and nanostructure-MB to either form a complex or degrade the MB, respectively, is happening.

3.5. Role of reactive oxygen species on the degradation mechanism of MB

The photocatalytic degradation mechanism by the MoO_3 nanostructures has been associated with the production of reactive oxygen species. In this study, the production of different ROS was evaluated for all three nanomaterials to better understand the degradation mechanisms of MoO_3 nanostructures under visible light. Figs. 8–10 represents the production of OH^- , $^1\text{O}_2$ and H_2O_2 radicals at different pH values, since pH clearly showed an important role in the photocatalytic activity of the MoO_3 nanostructures. Among the three different MoO_3 structures investigated, the nanorods produced the most ROS, which explains the increased photocatalytic activity of this nanomaterial as seen in Fig. 6. In fact, the presence of light directly affected the ROS production of the nanorods, as seen in Fig. S10.

More importantly, all three nanomaterials showed production of ROS even in dark conditions indicating that the nanomaterial not only have photocatalytic properties, but also catalytic properties. Production of ROS in the dark is not novel in photocatalytic

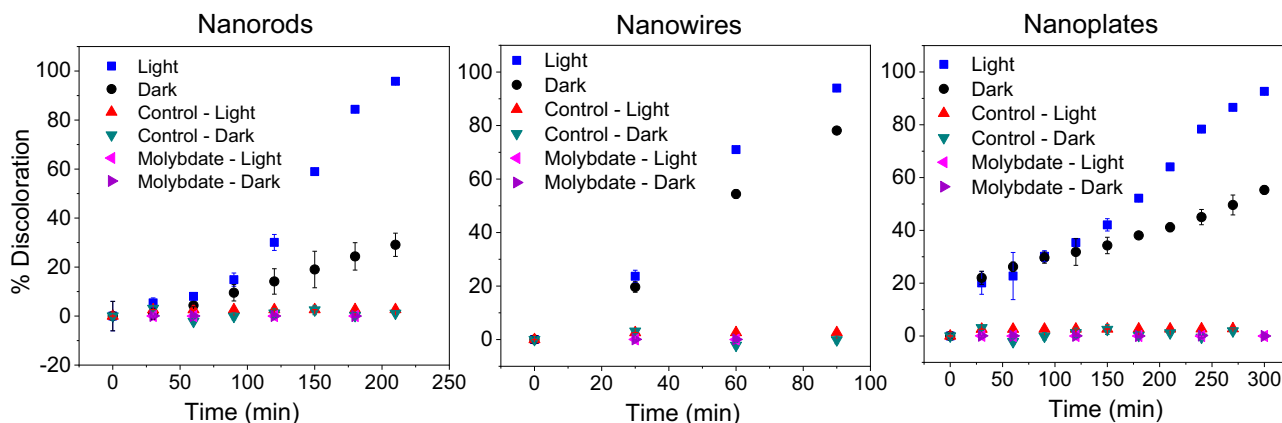


Fig. 6. Discoloration activity of different MoO₃ nanostructures at 500 mg/L with 50 mg/L of MB at pH 5.4. The dark samples correspond to ion-MB complexation and adsorption of the MB, while the light samples show adsorption, ion complexation, and photocatalytic activity of the nanostructures. The red and green samples correspond to the control experiment in which only MB was present. The purple and pink samples correspond to the control experiments in which only molybdate was present.

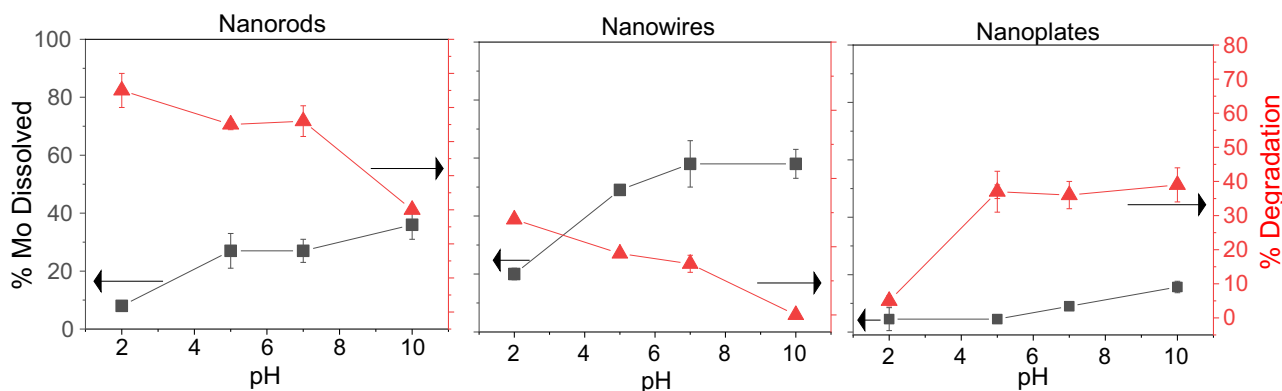


Fig. 7. Nanomaterial dissolution and MB degradation after light reaction after subtracting from dark reaction) at different pH values at the end of each experiment. The reactions were performed at 500 mg/L of MoO₃ nanostructures with 50 mg/L of MB. Black dots indicate the % of Mo dissolved and red dots the % of MB degraded.

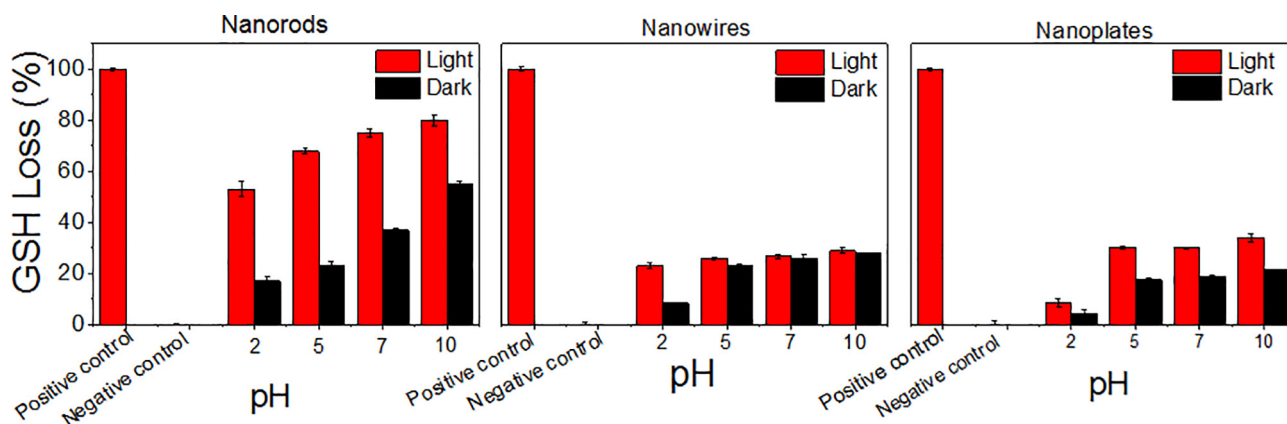


Fig. 8. Hydrogen peroxide production.

material as a number of studies report this phenomenon [65–67]. Furthermore, the production of ROS increased with increasing pH values. It is well-known that different radicals are produced at different pH values, and pH plays an important role in the generation of ROS. [68] Fig. S10 shows the contribution of ROS production due to the introduction of visible light for the different nanostructures at the different pH values. As we can see, the increase in pH increased the concentration of hydroxyl ions in solution, which can promote the formation of H₂O₂, following oxidation reactions

leading to the formation of singlet oxygen or undergoing reduction by forming hydroxyl radicals. The low amount formation of ¹O₂ can be explained because the singlet oxygen radical is not produced via electron transfer process [69].

Interestingly, if we compare the degradation results in Fig. 6 with the production of the ROS in Figs. 8–10, specifically the hydrogen peroxide production of the nanorods, nanowires, and nanoplates, we see similar patterns indicating that the most probable primary species responsible for the degradation of MB is hydrogen

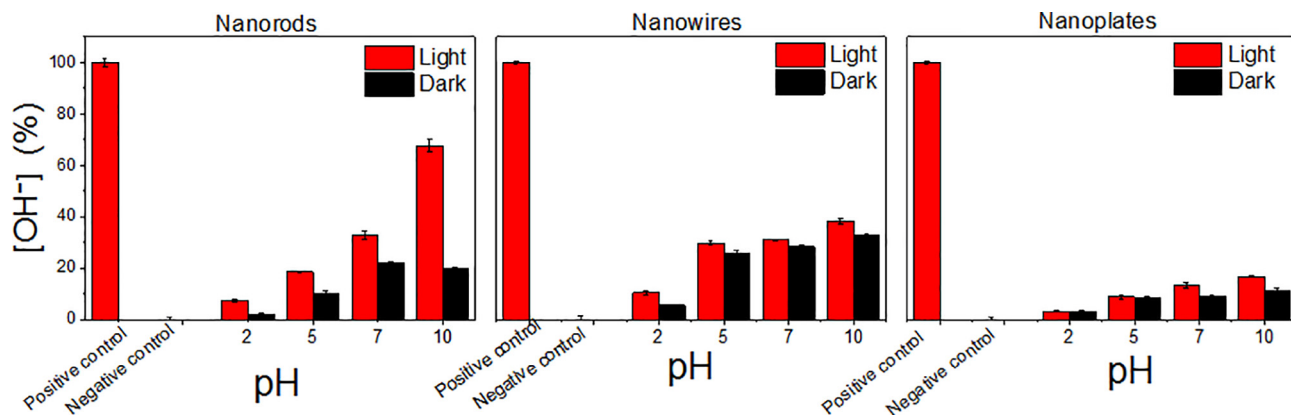


Fig. 9. Hydroxyl radical production.

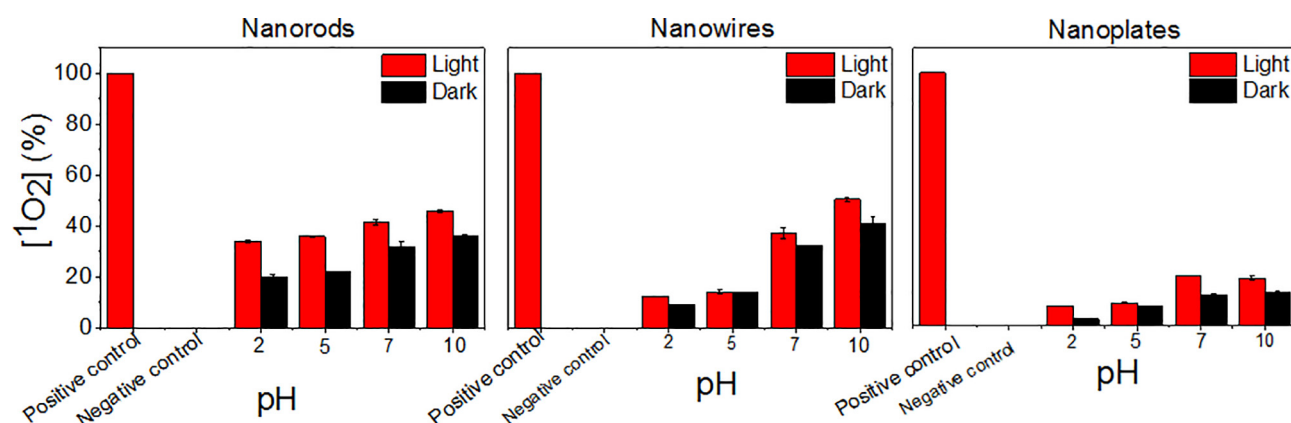


Fig. 10. Singlet oxygen production.

peroxide. For instance, with increasing pH, the hydrogen peroxide production contribution from the light by the nanorods and nanowires generally decreases as does the % degradation in Fig. 6. However, the hydrogen peroxide production of the nanoplates increases slightly and then remains approximately the same at pH 2, which corroborates the % degradation in Fig. 6, where the same pattern is observed.

The ROS from the isolated ions produced by the nanostructures were also evaluated in the present study. In Fig. S11, it is evident that the ion resulting from the dissolution of the nanomaterial can have degradative effects due to ROS production. In the dark condition, hydroxyl radical and hydrogen peroxide production were not significant, while in the presence of light, there was a significant increase in these ROS. This finding signifies that the dissolved ions from the nanomaterial can also contribute to the degradation of MB. ROS production by molybdate ion can undergo a Fenton-like reaction in water and produce ROS [70–73].

In order to further understand the role of ROS in the photocatalytic mechanism of the MoO₃ nanostructures, we employed ROS scavengers and a hole scavenger. Isopropyl alcohol (IPA) was employed to trap ·OH, triethanolamine (TEOA) scavenges h⁺ and benzoquinone (BQ) scavenges ·O₂⁻ [2,74–76]. These scavengers were added to the reaction and the degradation results are shown in Fig. 11.

The greatest effect in the presence of ROS scavengers was seen with the addition of TEOA, which is a hole scavenger, as shown in Fig. 11. Only with the presence of TEOA all three nanomaterials were unable to completely decolorize MB, indicating that the production of holes plays an important role in MB degradation. How-

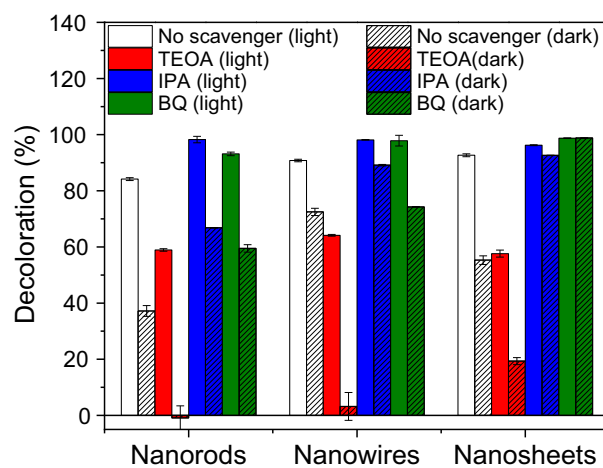


Fig. 11. MB degradation with each of the nanomaterial in the presence of scavengers in light and dark conditions. Reaction conditions were 500 mg/mL of MoO₃ at pH 5.4 in the presence of 10 mM of TEOA, 75 mM of IPA and 1 mM of p-BQ.

ever, when the reaction took place in the dark in the presence of TEOA, no discoloration was observed. In this case, TEOA seemed to act as a competing adsorbent able to inhibit the MB adsorption on the surface of the nanostructures. Furthermore, this confirms that the likely pathway by which hydrogen peroxide is generated is via the oxidation of water molecules by the photogenerated holes. In addition, hydrogen peroxide is the most likely primary

species responsible for the degradation of methylene blue since, when hydroxyl and singlet oxygen scavengers were added, complete degradation of MB was still possible. Interestingly, when isopropanol was present (a hydroxyl radical scavenger) the photocatalytic reaction became more efficient. A possible explanation could be that the generation of additional water molecules from the isopropanol and hydroxyl radical reaction may be oxidized by the photogenerated holes, further increasing hydrogen peroxide concentrations.

4. Conclusions

In the present work, we have successfully synthesized MoO₃ nanostructures with different sizes, morphologies, and properties. We have demonstrated that the dissolution process also depends on the oxidative state, and nature of the Mo–O bond. For instance, the nanoplates, which contained more Mo⁵⁺ than Mo⁶⁺, dissolved less than the nanorods which had more Mo⁶⁺ rather than Mo⁵⁺ in their structure. The dissolution process reported here shows that MoO₃ nanostructures are not suitable for most water treatment applications due to high solubility at the pH employed in drinking water. These results suggest that more research should be done in order to improve the stability of these nanostructures rather than present photocatalytic studies of different organic molecules. Given the limitations of this material it is not surprising that TiO₂ is more heavily utilized, as this nanomaterial is an extremely insoluble.

The photocatalytic experiments of methylene blue showed that the photocatalytic degradation of MB is influenced by the dissolution of the nanomaterials. Furthermore, there is a relationship between the degradation and complexation process. The dissolved ions can play an important role in the photocatalytic activity of the nanostructure. As shown in the HPLC experiments, the ion not only produces a complex between the MB, but it is also able to degrade MB.

While ROS production and subsequent degradation of MB were observed by the nanomaterial, some ROS production was observed by the dissolved product of the nanomaterial. We also quantified the production of different ROS and we saw that hydrogen peroxide is the most important ROS responsible for the degradation of MB. The analysis of the ROS and the employment of different scavengers showed that H₂O₂ and the photogenerated holes in the nanostructures play a role in the degradation process of methylene blue. The photogenerated holes increased the oxidation of water molecules while increasing the concentration of H₂O₂, the ROS responsible for the degradation of MB.

Funding

This work was supported by the NSF BEINM Grant Number: 1705511, and the Robert A. Welch Foundation award numbers (E-2011-20190330) and (E-1728). The findings achieved herein are solely the responsibility of the authors. Authors acknowledge Dr. Krakowiak and Mr. Raj Gopal for the BET measurements.

Declaration of Competing Interest

The authors declare that they have no known competing financial interests or personal relationships that could have appeared to influence the work reported in this paper.

Appendix A. Supplementary material

Supplementary data to this article can be found online at <https://doi.org/10.1016/j.jcat.2019.11.035>.

References

- [1] M. Santos-Beltran, F. Paraguay-Delgado, R. Garcia, W. Antunez-Flores, C. Ornelas-Gutierrez, A. Santos-Beltran, Fast methylene blue removal by MoO₃ nanoparticles, *J. Mater. Sci. Mater. Electron.* 28 (2017) 2935–2948, <https://doi.org/10.1007/s10854-016-5878-2>.
- [2] A. Chithambararaj, N.S. Sanjini, A.C. Bose, S. Velmathi, Flower-like hierarchical h-MoO₃: new findings of efficient visible light driven nano photocatalyst for methylene blue degradation, *Catal. Sci. Technol.* 3 (2013) 1405, <https://doi.org/10.1039/c3cy20764a>.
- [3] A. Manivel, G.J. Lee, C.Y. Chen, J.H. Chen, S.H. Ma, T.L. Horng, J.J. Wu, Synthesis of MoO₃ nanoparticles for azo dye degradation by catalytic ozonation, *Mater. Res. Bull.* 62 (2015) 184–191, <https://doi.org/10.1016/j.materresbull.2014.11.016>.
- [4] N. Pernicone, F. Lazzarin, G. Liberti, G. Lanzavecchia, The oxidation of methanol over pure MoO₃ catalyst, *J. Catal.* 14 (1969) 391–393, [https://doi.org/10.1016/0021-9517\(69\)90331-5](https://doi.org/10.1016/0021-9517(69)90331-5).
- [5] C.I. Fernandes, S.C. Capelli, P.D. Vaz, C.D. Nunes, Highly selective and recyclable MoO₃ nanoparticles in epoxidation catalysis, *Appl. Catal. A Gen.* 504 (2015) 344–350, <https://doi.org/10.1016/j.apcata.2015.02.027>.
- [6] P. Dwivedi, S. Dhanekar, S. Das, Synthesis of α -MoO₃ nano- flakes by dry oxidation of RF sputtered Mo thin films and their application in gas sensing, *Semicond. Sci. Technol.* 31 (n.d.) 1–7, doi:10.1088/0268-1242/31/11/115010.
- [7] R.B. Pujari, V.C. Lokhande, V.S. Kumbhar, N.R. Chodankar, C.D. Lokhande, Hexagonal microrods architected MoO₃ thin film for supercapacitor application, *J. Mater. Sci. Mater. Electron.* 27 (2016) 3312–3317, <https://doi.org/10.1007/s10854-015-4160-3>.
- [8] D.-T. Nguyen, S. Vedraïne, L. Cattin, P. Torchio, M. Morsli, F. Flory, J.C. Bernède, Effect of the thickness of the MoO₃ layers on optical properties of MoO₃/Ag/MoO₃ multilayer structures, *J. Appl. Phys.* 112 (2012), <https://doi.org/10.1063/1.4751334> 063505.
- [9] J.S. Chen, Y.L. Cheah, S. Madhavi, X.W. Lou, Fast synthesis of α -MoO₃ nanorods with controlled aspect ratios and their enhanced lithium storage, *Capabilities* (2010) 8675–8678.
- [10] C. Chaves-Lopez, H.N. Nguyen, R.C. Oliveira, E.T. Nadres, A. Paparella, D.F. Rodrigues, A morphological, enzymatic and metabolic approach to elucidate apoptotic-like cell death in fungi exposed to h- and α -molybdenum trioxide nanoparticles, *Nanoscale*. 10 (2018) 20702–20716, <https://doi.org/10.1039/c8nr06470a>.
- [11] X.W. Lou, H.C. Zeng, Hydrothermal synthesis of α -MoO₃ nanorods via acidification of ammonium heptamolybdate tetrahydrate, *Chem. Mater.* 14 (2002) 4781–4789, <https://doi.org/10.1021/cm0206237>.
- [12] A. Phuruangrat, D.J. Ham, S. Thongtem, J.S. Lee, Electrochemical hydrogen evolution over MoO₃ nanowires produced by microwave-assisted hydrothermal reaction, *Electrochem. Commun.* 11 (2009) 1740–1743, <https://doi.org/10.1016/j.elecom.2009.07.005>.
- [13] V. Kumar, X. Wang, P.S. Lee, Formation of hexagonal-molybdenum trioxide (h-MoO₃) nanostructures and their pseudocapacitive behavior, 7 11777 (2015), <https://doi.org/10.1039/c5nr01505g>.
- [14] E.P. Gray, C.L. Browning, M. Wang, K.D. Gion, E.Y. Chao, K.J. Koski, A.B. Kane, R. H. Hurt, Biodissolution and cellular response to MoO₃ nanoribbons and a new framework for early hazard screening for 2D materials, *Environ. Sci. Nano.* 5 (2018) 2545–2559, <https://doi.org/10.1039/c8en00362a>.
- [15] Z. Wang, W. Zhu, Y. Qiu, X. Yi, A. Von Dem Bussche, A. Kane, H. Gao, K. Koski, R. Hurt, Biological and environmental interactions of emerging two-dimensional nanomaterials, *Chem. Soc. Rev.* 45 (2016) 1750–1780, <https://doi.org/10.1039/c5cs00914f>.
- [16] H.N. Nguyen, E.T. Nadres, B.G. Alamani, D.F. Rodrigues, Designing polymeric adhesives for antimicrobial materials: poly(ethylene imine) polymer, graphene, graphene oxide and molybdenum trioxide—a biomimetic approach, *J. Mater. Chem. B* 5 (2017) 6616–6628, <https://doi.org/10.1039/c7tb00722a>.
- [17] S. Kittler, C. Greulich, J. Diendorf, M. Köller, M. Eppe, Toxicity of silver nanoparticles increases during storage because of slow dissolution under release of silver ions, *Chem. Mater.* 22 (2010) 4548–4554, <https://doi.org/10.1021/cm100023p>.
- [18] K. Loza, J. Diendorf, C. Sengstock, L. Ruiz-Gonzalez, J.M. Gonzalez-Calbet, M. Vallet-Regi, M. Köller, M. Eppe, The dissolution and biological effects of silver nanoparticles in biological media, *J. Mater. Chem. B* 2 (2014) 1634–1643, <https://doi.org/10.1039/c3tb21569e>.
- [19] W. Vogelsberger, Thermodynamic and Kinetic Considerations of the Formation and the Dissolution of Nanoparticles of Substances Having Low Solubility, *J. Phys. Chem. B* 107 (2003) 9669–9676, <https://doi.org/10.1021/jp030347z>.
- [20] E.A. Meulenkaamp, Size dependence of the dissolution of ZnO nanoparticles, *J. Phys. Chem. B* 102 (1998) 7764–7769, <https://doi.org/10.1021/jp982305u>.
- [21] T. Xia, M. Kovochich, M. Liong, M. Schowalter, A. Rosenauer, B. Gilbert, J.I. Zink, A.E. Nel, L. Mädler, Comparison of the mechanism of toxicity of zinc oxide and cerium oxide nanoparticles based on dissolution and oxidative stress properties, *Chem. Ing. Tech.* 81 (2009) 1167, <https://doi.org/10.1002/cite.200950629>.
- [22] S.K. Misra, A. Dybowska, D. Berhanu, S.N. Luoma, E. Valsami-Jones, The complexity of nanoparticle dissolution and its importance in nanotoxicological studies, *Sci. Total Environ.* 438 (2012) 225–232, <https://doi.org/10.1016/j.scitotenv.2012.08.066>.
- [23] D. Wang, L. Zhao, L.H. Guo, H. Zhang, Online Detection of reactive oxygen species in ultraviolet (UV)-irradiated nano-TiO₂ suspensions by continuous

- flow chemiluminescence, *Anal. Chem.* 86 (2014) 10535–10539, <https://doi.org/10.1021/ac503213m>.
- [24] Y. Nosaka, A.Y. Nosaka, Generation and detection of reactive oxygen species in photocatalysis, *Chem. Rev.* 117 (2017) 11302–11336, <https://doi.org/10.1021/acs.chemrev.7b00161>.
- [25] Y. Guo, C. Cheng, J. Wang, Z. Wang, X. Jin, K. Li, P. Kang, J. Gao, Detection of reactive oxygen species (ROS) generated by TiO₂(R), TiO₂(R/A) and TiO₂(A) under ultrasonic and solar light irradiation and application in degradation of organic dyes, *J. Hazard. Mater.* 192 (2011) 786–793, <https://doi.org/10.1016/j.jhazmat.2011.05.084>.
- [26] Y. Li, W. Zhang, J. Niu, Y. Chen, Mechanism of photogenerated reactive oxygen species and correlation with the antibacterial properties of engineered metal-oxide nanoparticles, *ACS Nano*. 6 (2012) 5164–5173, <https://doi.org/10.1021/nn300934k>.
- [27] A.S. Adeleye, X. Wang, F. Wang, R. Hao, W. Song, Y. Li, Photoreactivity of graphene oxide in aqueous system: reactive oxygen species formation and bisphenol A degradation, *Chemosphere* 195 (2018) 344–350, <https://doi.org/10.1016/j.chemosphere.2017.12.095>.
- [28] O. Choi, Z. Hu, Size dependent and reactive oxygen species related nanosilver toxicity to nitrifying bacteria, *Environ. Sci. Technol.* 42 (2008) 4583–4588, <https://doi.org/10.1021/es703238h>.
- [29] M.J. Akhtar, M. Ahamed, S. Kumar, M.A. Majeed Khan, J. Ahmad, S.A. Alrokayan, Zinc oxide nanoparticles selectively induce apoptosis in human cancer cells through reactive oxygen species, *Int. J. Nanomed.* 7 (2012) 845–857, <https://doi.org/10.2147/IJN.S29129>.
- [30] K. Buyukhatipoglu, A.M. Clyne, Superparamagnetic iron oxide nanoparticles change endothelial cell morphology and mechanics via reactive oxygen species formation, *J. Biomed. Mater. Res. - Part A*. 96A (2011) 186–195, <https://doi.org/10.1002/jbm.a.32972>.
- [31] A. Chithambararaj, A.C. Bose, Hydrothermal synthesis of hexagonal and orthorhombic MoO₃ nanoparticles, *J. Alloys Compd.* 509 (2011) 8105–8110, <https://doi.org/10.1016/j.jallcom.2011.05.067>.
- [32] H. Yin, Y. Kuwahara, K. Mori, H. Cheng, M. Wen, Y. Huo, H. Yamashita, Localized surface plasmon resonances in plasmonic molybdenum tungsten oxide hybrid for visible-light-enhanced catalytic reaction, *J. Phys. Chem. C* 121 (2017) 23531–23540, <https://doi.org/10.1021/acs.jpcc.7b08403>.
- [33] Y. Chen, C. Lu, L. Xu, Y. Ma, W. Hou, J.J. Zhu, Single-crystalline orthorhombic molybdenum oxide nanobelts: synthesis and photocatalytic properties, *CrystrEngComm*. 12 (2010) 3740–3747, <https://doi.org/10.1039/c000744g>.
- [34] J. Peña-Bahamonde, V. San Miguel, H.N. Nguyen, R. Ozisik, D.F. Rodrigues, J.C. Cabanelas, Functionalization of reduced graphene oxide with polysulfone brushes enhance antibacterial properties and reduce human cytotoxicity, *Carbon* N. Y. 111 (2017) 258–268, <https://doi.org/10.1016/j.carbon.2016.10.005>.
- [35] J. Fan, Y. Li, H.N. Nguyen, Y. Yao, D.F. Rodrigues, Toxicity of exfoliated-MoS₂ and annealed exfoliated-MoS₂ towards planktonic cells, biofilms, and mammalian cells in the presence of electron donor, *Environ. Sci. Nano* 2 (2015) 370–379, <https://doi.org/10.1039/C5EN00031A>.
- [36] D. Jassby, J. Farner Budarz, M. Wiesner, Impact of aggregate size and structure on the photocatalytic properties of TiO₂ and ZnO nanoparticles, *Environ. Sci. Technol.* 46 (2012) 6934–6941, <https://doi.org/10.1021/es202009h>.
- [37] X. Xu, D. Chen, Z. Yi, M. Jiang, L. Wang, Z. Zhou, X. Fan, Y. Wang, D. Hui, Antimicrobial mechanism based on H₂O₂ generation at oxygen vacancies in ZnO crystals, *Langmuir* 29 (2013) 5573–5580, <https://doi.org/10.1021/la400378t>.
- [38] A. Abdal Dayem, M.K. Hossain, S. Bin Lee, K. Kim, S.K. Saha, G.-M. Yang, H.Y. Choi, S.-G. Cho, The role of reactive oxygen species (ROS) in the biological activities of metallic nanoparticles, *Int. J. Mol. Sci.* 18 (2017) 120, <https://doi.org/10.3390/ijms18010120>.
- [39] W.R. Haag, J. Hoigne, E. Gassman, A. Braun, Singlet oxygen in surface waters – Part I: Furfuryl alcohol as a trapping agent, *Chemosphere* 13 (1984) 631–640, [https://doi.org/10.1016/0045-6535\(84\)90199-1](https://doi.org/10.1016/0045-6535(84)90199-1).
- [40] M.A. Rauf, M. Meetani, A. Khaleel, Photocatalytic degradation of methylene blue using a mixed catalyst and product analysis by LC/MS (2010) doi:10.1016/j.cej.2009.11.017.
- [41] S.B. Rathod, M.K. Lande, B.R. Arbad, A.B. Gambhire, Preparation, characterization and catalytic activity of MoO₃/CeO₂-ZrO₂ solid heterogeneous catalyst for the synthesis of β-enaminones, *Arab. J. Chem.* 7 (2014) 253–260, <https://doi.org/10.1016/j.arabjc.2010.10.027>.
- [42] D. Sundeep, A. Gopala Krishna, R.V.S.S.N. Ravikumar, T. Vijaya Kumar, S. Daniel Ephraim, Y.L. Pavan, Spectral characterization of mechanically synthesized MoO₃-CuO nanocomposite, *Int. Nano Lett.* 6 (2016) 119–128, <https://doi.org/10.1007/s40089-015-0178-z>.
- [43] A. Monshi, M.R. Foroughi, M.R. Monshi, Modified Scherrer equation to estimate more accurately nano-crystallite size using XRD, *World J. Nano Sci. Eng.* 02 (2012) 154–160, <https://doi.org/10.4236/wjnse.2012.23020>.
- [44] S. Enzo, G. Fagherazzi, A. Benedetti, S. Polizzi, A profile-fitting procedure for analysis of broadened X-ray diffraction peaks. I. Methodology, *J. Appl. Crystallogr.* 21 (1988) 536–542, <https://doi.org/10.1107/S0021888888006612>.
- [45] T. Ungár, S. Ott, P. Sanders, A. Borbély, J. Weertman, Dislocations, grain size and planar faults in nanostructured copper determined by high resolution X-ray diffraction and a new procedure of peak profile analysis, *Acta Mater.* 46 (1998) 3693–3699, [https://doi.org/10.1016/S1359-6454\(98\)00001-9](https://doi.org/10.1016/S1359-6454(98)00001-9).
- [46] G.A. Nazri, C. Julien, Far-infrared and Raman studies of orthorhombic MoO₃ single crystal, *Solid State Ionics* 53–56 (1992) 376–382, [https://doi.org/10.1016/0167-2738\(92\)90403-C](https://doi.org/10.1016/0167-2738(92)90403-C).
- [47] T. Hirata, In-situ observation of Mo-O stretching vibrations during the reduction of MoO₃ with hydrogen by diffuse reflectance FTIR spectroscopy, *Appl. Surf. Sci.* 40 (1989) 179–181, [https://doi.org/10.1016/0169-4332\(89\)90174-8](https://doi.org/10.1016/0169-4332(89)90174-8).
- [48] W.P. Griffith, Oxy-complexes and their vibrational spectra, *J. Chem. Soc. A Inorganic, Phys. Theor.* 211 (1969), <https://doi.org/10.1039/j19690000211>.
- [49] R. Nadimicherla, W. Chen, X. Guo, Synthesis and characterization of α-MoO₃ nanobelt composite positive electrode materials for lithium battery application, *Mater. Res. Bull.* 66 (2015) 140–146, <https://doi.org/10.1016/j.materresbull.2015.02.036>.
- [50] K. Inzani, M. Nematollahi, F. Vullum-Bruer, T. Grande, T.W. Reenaas, S.M. Selbach, Electronic properties of reduced molybdenum oxides, *Phys. Chem. Chem. Phys.* 19 (2017) 9232–9245, <https://doi.org/10.1039/c7cp00644f>.
- [51] S. Zhu, D. Wang, Photocatalysis: basic principles, diverse forms of implementations and emerging scientific opportunities, *Adv. Energy Mater.* 7 (2017), <https://doi.org/10.1002/aenm.201700841>.
- [52] H. Cheng, T. Kamegawa, K. Mori, H. Yamashita, Surfactant-free nonaqueous synthesis of plasmonic molybdenum oxide nanosheets with enhanced catalytic activity for hydrogen generation from ammonia borane under visible light, *Angew. Chem. - Int. Ed.* 53 (2014) 2910–2914, <https://doi.org/10.1002/anie.201309759>.
- [53] H. Cheng, X. Qian, Y. Kuwahara, K. Mori, H. Yamashita, A Plasmonic molybdenum oxide hybrid with reversible tunability for visible-light-enhanced catalytic reactions, *Adv. Mater.* 27 (2015) 4616–4621, <https://doi.org/10.1002/adma.201501172>.
- [54] B.F. Sels, D.E. De Vos, P.J. Grobet, F. Pierard, F. Kirsch-De Mesmaeker, P.A. Jacobs, Molybdate- and tungstate-exchanged layered double hydroxides as catalysts for I₂ formation: characterization of reactive oxygen species and a critical evaluation of I₂ detection methods, *J. Phys. Chem. B* 103 (1999) 11114–11123, <https://doi.org/10.1021/jp992236z>.
- [55] T. Ozeki, H. Kihara, S. Ikeda, Study of equilibrium in 0.03 mM molybdate acidic aqueous solutions by factor analysis applied to ultraviolet spectra, *Anal. Chem.* 60 (1988) 2055–2059, <https://doi.org/10.1021/ac00170a014>.
- [56] W. Swartz, D.M. Hercules, X-ray photoelectron spectroscopy of molybdenum compounds. Use of electron spectroscopy for chemical analysis (ESCA) in quantitative analysis, *Anal. Chem.* 43 (1971) 1774–1779, <https://doi.org/10.1021/ac60307a020>.
- [57] G. Davis, W.C. Moshier, G.D. Davis, Interaction of molybdate anions with the passive film on aluminum (2015). doi:10.5006/1.3585065.
- [58] J.-G. Choi, L.T. Thompson, XPS study of as-prepared and reduced molybdenum oxides, *Appl. Surf. Sci.* 93 (1996) 143–149, [https://doi.org/10.1016/0169-4332\(95\)00317-7](https://doi.org/10.1016/0169-4332(95)00317-7).
- [59] P.C. Chen, S.J. Hsieh, C.C. Chen, J. Zou, The microstructure and capacitance characterizations of anodic titanium based alloy oxide nanotube, *J. Nanomater.* 2013 (2013), <https://doi.org/10.1155/2013/157494>.
- [60] A. Aracena, A. Sanino, O. Jerez, Dissolution kinetics of molybdate in KOH media at different temperatures, *Trans. Nonferrous Met. Soc. China (English Ed.)* 28 (2018) 177–185, [https://doi.org/10.1016/S1003-6326\(18\)64651-5](https://doi.org/10.1016/S1003-6326(18)64651-5).
- [61] J. Aveston, E.W. Anacker, J.S. Johnson, Hydrolysis of molybdenum(VI). Ultracentrifugation, acidity measurements, and raman spectra of polymolybdates, *Inorg. Chem.* 3 (1964) 735–746, <https://doi.org/10.1021/ic50015a030>.
- [62] R.H. Busey, O.L. Keller, Structure of the aqueous pertechnetate ion by Raman and infrared spectroscopy. Raman and infrared spectra of Crystalline K₂CrO₄, K₂ReO₄, Na₂MoO₄, Na₂WO₄, Na₂MoO₄·2H₂O, and Na₂WO₄·2H₂O, *J. Chem. Phys.* 41 (1964) 215–225, <https://doi.org/10.1063/1.1725625>.
- [63] V.A. Petrochenkov, I.G. Gorichev, V.V. Batrakov, A.D. Izotov, A.M. Kutepov, Catalytic effect of ammonia on the kinetics and mechanism of MoO₃ dissolution in alkaline solutions, *Theor. Found. Chem. Eng.* 38 (2004) 386–393, <https://doi.org/10.1023/B:TFCE.0000036965.59052.20>.
- [64] M.A. Rauf, M. Meetani, A. Khaleel, M.A. Rauf, M.A. Meetani, A. Khaleel, A. Ahmed, Photocatalytic degradation of methylene blue using a mixed catalyst and product analysis by LC/MS, *Artic. Chem. Eng. J.* 157 (2010) 373–378, <https://doi.org/10.1016/j.cej.2009.11.017>.
- [65] V. Lakshmi Prasanna, V. Rajagopalan, A new synergetic nanocomposite for dye degradation in dark and light, *Sci. Rep.* 6 (1) (2016), <https://doi.org/10.1038/srep38606>.
- [66] V.W. Hei Lau, D. Klose, H. Kasap, F. Podjaski, M.C. Pignié, E. Reisner, G. Jeschke, B.V. Lotsch, Dark photocatalysis: storage of solar energy in carbon nitride for time-delayed hydrogen generation, *Angew. Chem. - Int. Ed.* 56 (2017) 510–514, <https://doi.org/10.1002/anie.201608553>.
- [67] V. Lakshmi Prasanna, R. Vijayaraghavan, Insight into the mechanism of antibacterial activity of ZnO: surface defects mediated reactive oxygen species even in the dark, *Langmuir* 31 (2015) 9155–9162, <https://doi.org/10.1021/acs.langmuir.5b02266>.
- [68] A. Ahmad, X. Gu, L. Li, S. Lu, Y. Xu, X. Guo, Effects of pH and anions on the generation of reactive oxygen species (ROS) in nZVI-rGo-activated persulfate system, *Water. Air. Soil Pollut.* 226 (2015), <https://doi.org/10.1007/s11270-015-2635-8>.
- [69] H. Xu, W.J. Cooper, J. Jung, W. Song, Photosensitized degradation of amoxicillin in natural organic matter isolate solutions, *Water Res.* 45 (2011) 632–638, <https://doi.org/10.1016/j.watres.2010.08.024>.
- [70] I. Popivker, I. Zilbermann, E. Maimon, H. Cohen, D. Meyerstein, The “fenton like” reaction of MoO₄²⁻ involves two H₂O₂ molecules, *Dalt. Trans.* 42 (2013) 16666–16668, <https://doi.org/10.1039/c3dt52333k>.

- [71] B.F. Sels, D.E. De Vos, P.J. Grobet, F. Pierard, F. Kirsch-De Mesmaeker, P.A. Jacobs, Molybdate-and tungstate-exchanged layered double hydroxides as catalysts for H_2O_2 formation: characterization of reactive oxygen species and a critical evaluation of H_2O_2 detection methods (1999). doi:10.1021/jp992236z.
- [72] M.M. Rashad, A.A. Ibrahim, D.A. Rayan, M.M.S. Sanad, I.M. Helmy, Photo-Fenton-like degradation of Rhodamine B dye from waste water using iron molybdate catalyst under visible light irradiation, *Environ. Nanotechnology, Monit. Manag.* 8 (2017) 175–186, <https://doi.org/10.1016/j.enmm.2017.07.009>.
- [73] S. Tian, J. Zhang, J. Chen, L. Kong, J. Lu, F. Ding, Y. Xiong, $\text{Fe}_2(\text{MoO}_4)_3$ as an effective photo-fenton-like catalyst for the degradation of anionic and cationic dyes in a wide pH range, *Ind. Eng. Chem. Res.* 52 (2013) 13333–13341, <https://doi.org/10.1021/ie401522a>.
- [74] M. Zhong, Z. Wei, X. Meng, F. Wu, J. Li, From MoS_2 microspheres to $\alpha\text{-MoO}_3$ nanoplates: growth mechanism and photocatalytic activities, *Eur. J. Inorg. Chem.* 2015 (2014) 3245–3251, <https://doi.org/10.1002/ejic.201402079>.
- [75] Z. Liu, Y. Jin, F. Teng, X. Hua, M. Chen, An efficient Ce-doped MoO_3 catalyst and its photo-thermal catalytic synergetic degradation performance for dye pollutant, *CATCOM* 66 (2015) 42–45, <https://doi.org/10.1016/j.catcom.2015.03.017>.
- [76] Y. Liu, P. Feng, Z. Wang, X. Jiao, F. Akhtar, Novel fabrication and enhanced photocatalytic MB degradation of hierarchical porous monoliths of MoO_3 Nanoplates, *Sci. Rep.* 7 (2017), <https://doi.org/10.1038/s41598-017-02025-3>.